

不同热处理工艺下增材制造 TC17 钛合金组织与摩擦学性能研究

王浩^{1*}, 胡怡宁², 王涛²¹中国民航大学工程技术训练中心, 天津 300300;²中国民航大学航空工程学院, 天津 300300

摘要 研究了不同热处理工艺对定向能量沉积 TC17 钛合金微观组织与摩擦学性能的影响, 分析了热处理过程中的组织演变规律与 20 N 干滑动磨损下的综合磨损行为。结果表明, 在退火与退火后固溶处理阶段, 合金主要由初生 α 相及连续或不连续的晶界 α 相、 β 相组成, 无相析出区伴随连续晶界 α 相存在。在退火后固溶处理的基础上进一步进行时效处理, 针状次生 α 相开始析出, 且随着时效温度的升高, 初生与次生 α 相开始生长、粗化, 无相析出区先消失后出现。硬度与磨损测试结果表明, 经 580 °C 时效处理后显微硬度最高 (486.93 HV), 此时有较强的弥散强化效果, 摩擦学性能最优, 磨损率仅为 0.0451 mg/m。热处理后多种磨损机制混合存在, 磨损率、磨损形貌取决于微观结构与氧化层的变化。研究结果为优化 TC17 合金摩擦学性能与热处理工艺提供了参考。

关键词 激光技术; 钛合金; 摩擦学性能; 微观组织; 热处理; 定向能量沉积

中图分类号 TG146.2+3

文献标志码 A

DOI: 10.3788/CJL231043

1 引言

钛及钛合金具有高比强度、高抗疲劳性和良好的生物相容性等众多优异性能, 是应用于航空航天领域的增材热门材料^[1-2]。TC17 合金 (Ti-5Al-2Sn-2Zr-4Mo-4Cr) 具有优异的机械强度^[3]、断裂韧性^[4-6]与突出的耐腐蚀性^[7], 能够满足损伤容限设计的需要^[8], 主要用于制造航空发动机风扇盘、压气机盘等盘类构件^[9-10]。定向能量沉积 (DED) 技术能够实现受损零件的特定位置修复及复杂几何形状部件与大型部件的三维打印^[11-12], 其中定向能量沉积的 TC17 合金已被成功应用在整体叶盘等关键部件中^[13]。然而, 由于 TC17 合金硬度低、耐磨性差的特性, 在航空发动机恶劣的使用环境下冲刷磨损易引发疲劳断裂, 限制了其在航空航天领域中的应用^[14]。目前, 在钛合金表面喷涂硬质涂层是解决钛合金硬度低、耐磨性差的有效手段之一^[15], 但涂覆涂层存在结合力差、引入新缺陷、不能满足多种性能要求等问题^[16-17]。

优化热处理的方法能够通过调整微观结构来调整材料性能。Zhu 等^[18]研究了退火温度对 TC17 合金组织演变和拉伸性能的影响, 结果表明, 在 $\alpha + \beta$ 相区或单 β 相区, 退火处理可改善增材 TC17 的力学性能。Zhang 等^[19]分析了退火处理下增材 TC17 不同尺寸试

样的组织、硬度与拉伸性能, 发现 5 mm 厚样品的硬度随退火时间的延长而降低, 25 mm 厚样品的硬度变化不大, 与 T 向 (垂直于沉积方向) 试样相比, L 向 (平行于沉积方向) 试件的拉伸性能表现出强度低、塑性高的特点。陈博等^[20]研究了退火和固溶时效处理对激光熔化沉积 TC17 显微组织与力学性能的影响, 结果表明, 经过 800 °C/4 h、水淬 + 630 °C/8 h、空冷处理后, 强塑性匹配达到最佳, 可满足盘类拉伸测试技术标准。崔广发等^[21]研究了点式锻造激光沉积 TC17 热处理后的性能, 发现经过 730 °C 退火后, 各向异性降低, 强度与塑性达到使用标准。Elshaer 等^[22]研究了多种热处理工艺对锻造 TC4 摩擦学性能的影响, 结果表明, 相较于固溶处理, 固溶 (水淬) 后的时效处理使耐磨性提高了大约 125%。Su 等^[2]对激光粉末床熔融 TC4 合金进行了直接时效与固溶时效处理以提高其摩擦学性能, 结果表明, 固溶时效可以获得更高的初始硬度与更有利的时效硬化响应, 从而进一步增强耐磨性。通过优化热处理工艺, 调节 TC17 微观组织, 从而改善拉伸性能的研究较多, 而改善耐磨性的研究主要集中在 TC4^[23-26], 关于优化热处理是否能改善沉积 TC17 合金的耐磨性还需要进一步研究。

本文研究了预退火、退火后固溶、退火后固溶时效处理对沉积 TC17 合金微观结构、硬度与摩擦学性能

收稿日期: 2023-07-21; 修回日期: 2023-08-14; 录用日期: 2023-09-07; 网络首发日期: 2023-09-15

基金项目: 国家自然科学基金 (U2133202)、四川省重大科技专项项目 (2021ZDZX0001)、研究生科技创新基金 (2022YJS058)

通信作者: hbgdwh@vip.126.com

的影响。采用 X 射线衍射 (XRD) 与扫描电子显微镜 (SEM) 对 TC17 合金热处理过程中的组织演变进行了分析。在 20 N 载荷下进行了干滑动磨损测试, 结合白光干涉仪与能量色散 X 射线谱 (EDS), 深入研究了热处理对磨损形貌与磨损机制的影响。

2 实验材料与方法

2.1 材料及过程

TC17 球形粉末采用真空等离子体旋转电极雾化方式制备, 其流动性为 19.7 s/50 g, 粉末形貌如图 1(a) 所示, 粒度分布如图 1(b) 所示, 平均粒度为 66.6 μm , 其化学成分如表 1 所示。实验前为消除干

扰因素, 将 TC17 粉末在 110 $^{\circ}\text{C}$ 的恒温干燥室中处理 1.5 h。

本文使用半导体激光器 [中心波长为 (915 \pm 10) nm, 最大功率为 3000 W, 光斑直径为 4 mm] 产生激光, 配备同轴送粉的机器人, 在氩气环境中将 TC17 粉末沉积在抛光后的 TC4 基板 (尺寸为 240 mm \times 120 mm \times 20 mm) 上。优化工艺参数为: 激光功率为 1600 W, 扫描速度为 10 mm/s, 送粉率为 11 g/min, 搭接率为 45%, 中心保护气流量为 11 L/min, 采用“N”形扫描路径获得 TC17 合金试样 (尺寸为 75 mm \times 35 mm \times 12 mm)。沉积过程如图 2 所示。沿激光沉积方向取样, 样品尺寸为 6 mm \times 6 mm \times 6 mm。

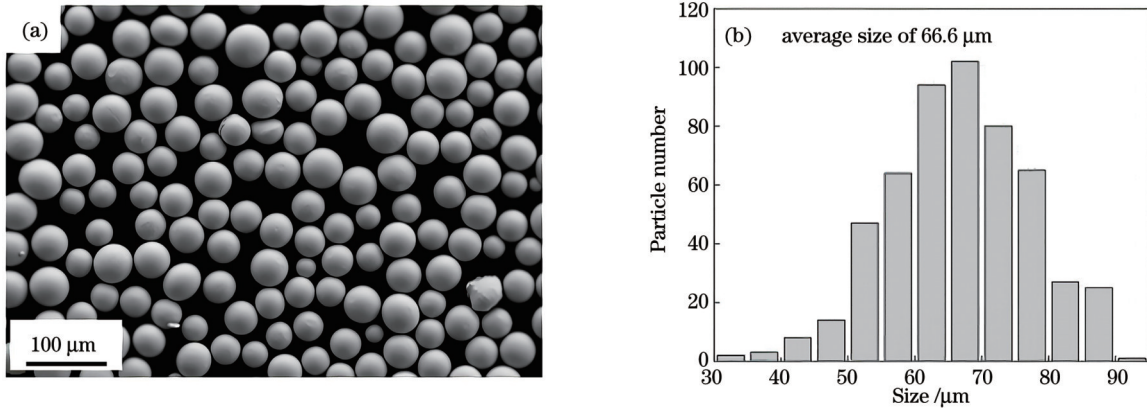


图 1 TC17 合金粉末的形貌与粒度分布。(a) 形貌; (b) 粒度分布

Fig. 1 Morphology and particle size distribution of TC17 alloy powder. (a) Morphology; (b) particle size distribution

表 1 TC17 合金粉末的化学成分 (质量分数, %)

Table 1 Chemical compositions of TC17 alloy powder (mass fraction, %)

Powder	Al	Sn	Zr	Mo	Cr	Fe	O	Ti
TC17	5.06	2.10	1.97	3.96	4.00	0.22	0.11	Bal.

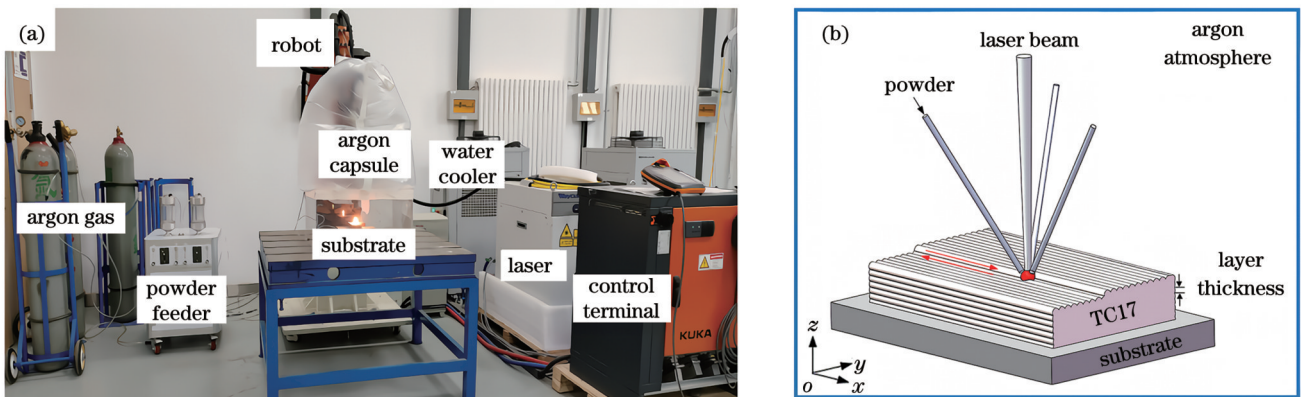


图 2 DED 过程。(a) 实验环境; (b) TC17 合金沉积过程

Fig. 2 DED process. (a) Experimental environment; (b) TC17 alloy deposition process

参考已有的 TC17 热处理研究^[18-20], 对 TC17 沉积试样进行退火、固溶处理后, 分别进行不同温度下的时效处理, 图 3 为 5 组热处理制度的具体过程。第一阶段, 退火预处理, 即在 840 $^{\circ}\text{C}$ 下保温 1 h, 空冷 (AC) 至室温, 初步调整 α 相的体积分数; 第二阶段,

固溶处理, 即在 800 $^{\circ}\text{C}$ 下保温 4 h, 水淬 (WQ) 至室温, 进一步调整初生 α 相 (α_p) 的尺寸; 第三阶段, 时效处理, 即分别在 580、630、680 $^{\circ}\text{C}$ 下保温 8 h, 空冷至室温, 研究次生 α 相 (α_s) 的析出和生长对硬度与磨损性能的影响。

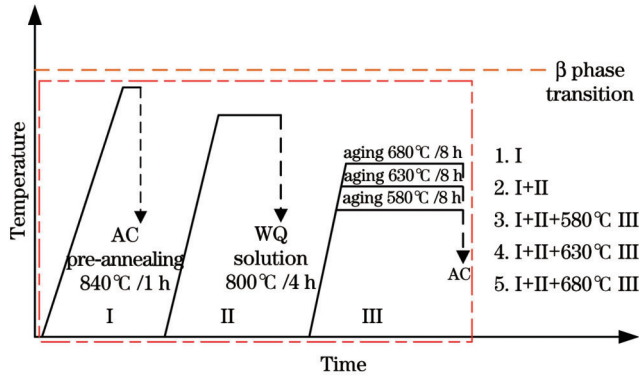


图 3 TC17合金热处理工艺
Fig. 3 Heat treatment process of TC17 alloy

2.2 微观结构表征与摩擦实验

采用X射线衍射仪(Cu源,最大电压为40 kV,最大电流为140 mA)进行相组成分析,衍射角(2θ)为 $10^\circ\sim 90^\circ$,步长为 0.02° ,扫描速度为 $1^\circ/\text{min}$ 。采用标准金相工艺对TC17样品进行抛光,用Kroll试剂(HF 、 HNO_3 、 H_2O 的体积比为1:3:50)进行60 s化学蚀刻。采用配备EDS的扫描电镜(SEM)进行微观结构观察与元素分析。使用维氏硬度计测量样品截面硬度,每间隔 $50\ \mu\text{m}$ 测量一次,设定载荷为200 g,停留时间为10 s,测量三次取均值。采用销盘式摩擦磨损试验机(图4)进行室温干滑动磨损实验,对磨金属球是直径为6 mm的钢球。摩擦磨损实验中法向载荷(F_N)为20 N,

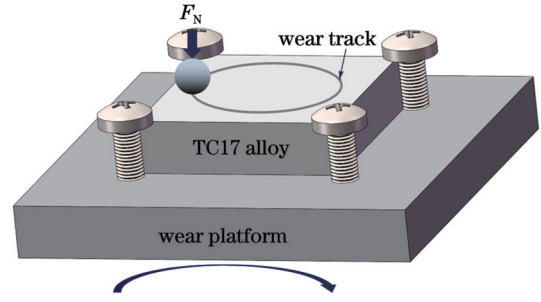


图 4 销盘磨损示意图
Fig. 4 Pin disc wear diagram

转速为300 r/min,摩擦半径为1.5 mm,测试时间为45 min。实验结束后,采用垂直扫描分辨率为0.1 nm的白光干涉仪进行磨损轨迹截面轮廓的测量,根据磨损率与轨迹分析样品的磨损性能。

3 分析与讨论

3.1 相分析

沉积及热处理样品的XRD谱如图5所示,可以观察到样品的主要组成为 α -Ti和 β -Ti相。定向能量沉积的急冷急热与熔池的快速凝固导致了非平衡的马氏体相变,一些 β 相晶格结构发生了改变但未及时析出 α 相,形成了 α' 马氏体与 α 平衡态共存的微观组织,随着热处理的进行,亚稳 α' 马氏体逐渐分解,相组成变为平衡($\alpha+\beta$)相^[27-28],表现出强的 α 与 β 衍射峰。

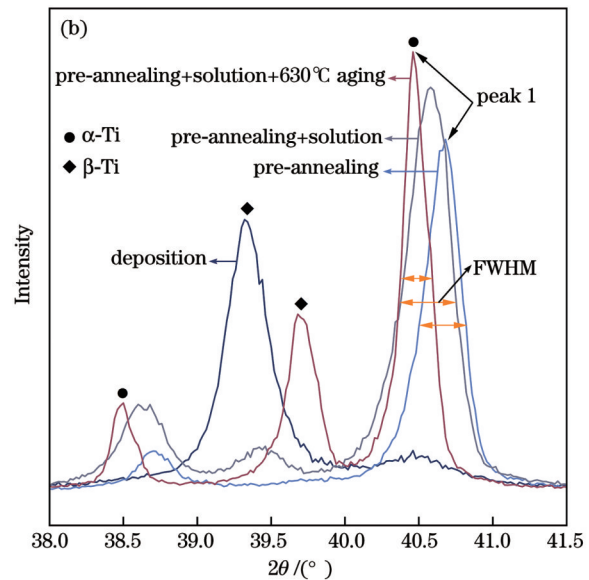
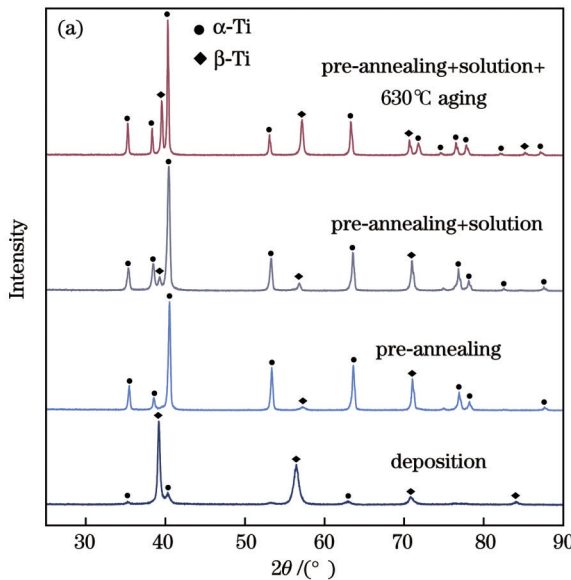


图 5 TC17合金XRD谱。(a) $2\theta=30^\circ\sim 90^\circ$; (b)图5(a)的局部放大
Fig. 5 XRD spectra of TC17 alloy. (a) $2\theta=30^\circ\sim 90^\circ$; (b) local magnification of Fig. 5(a)

图5(b)是图5(a)的局部放大,表2总结了图5(b)中peak 1处 2θ 与半峰全宽(FWHM, F_w)的关系,清楚地展示了衍射峰强度与位置的变化。热处理中合金元素的溶解与析出会影响 2θ 的位置,沉积形成的 α' 马氏体被自然压缩,晶格参数比 α 平衡态小, α' 马氏体的分解导致peak 1处的 2θ 位置不断左移,峰向小角度方向

表 2 peak 1处 2θ 与FWHM
Table 2 2θ and FWHM at peak 1

Sample	$2\theta / (^\circ)$	FWHM
Pre-annealing	40.68	0.30
Pre-annealing+Solution	40.58	0.36
Pre-annealing+Solution+630°C Aging	40.46	0.21

偏移。在 peak 1 处 FWHM 的变化范围为 0.21~0.36, 其变化与晶粒尺寸密切相关。Scherrer 公式^[29]为

$$L = K\lambda / (F_w \cos \theta), \quad (1)$$

式中: L 为平均晶粒尺寸; K 为与微晶形状相关的常数, 通常取 0.9; λ 为 X 射线波长。平均晶粒尺寸与 FWHM 成反比, 证实经 630 °C 时效处理后平均晶粒尺寸大于退火与固溶处理。

3.2 微观结构

图 6 给出了 TC17 沉积态的显微组织。从微观上

看, TC17 合金由 α 与 β 相组成, 呈现网篮组织。利用 Image-Pro Plus 软件进行定量分析, 三次统计后取均值, 确定 α 板条平均长度为 1.28 μm , 均宽为 0.26 μm , 体积分数为 67.9%。在不同工艺参数下, 沉积态 TC17 的相尺寸与含量也有区别。此外, TC17 作为近 β 钛合金, 具有典型择优形核的连续晶界 α 相 (α_{GB}) 微观特征, 其是低延展性的根源^[30], 沉积态中连续 α_{GB} 宽度为 0.58 μm , 远比晶内 α 板条宽, 通过热处理可以适当改变 α_{GB} 形貌, 平衡 TC17 的力学性能。

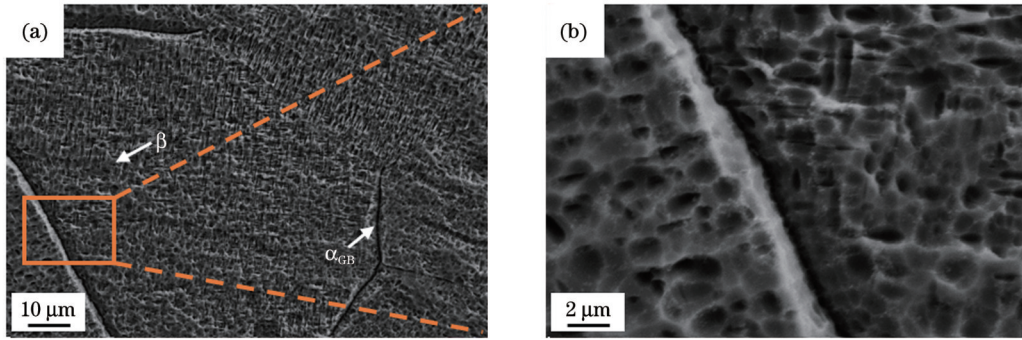


图 6 沉积态 TC17 的微观结构。(a) 微观组织; (b) 图 6(a) 的局部放大

Fig. 6 Microstructure of as-deposited TC17. (a) Microstructure; (b) local magnification of Fig. 6(a)

在低于 β 相变点的温度下对沉积试样进行热处理, 退火和退火后固溶的微观组织如图 7 所示。经

840 °C 预退火后, 受高温影响, 部分细小 α 相溶解, 相对较宽的板条 α 相开始生长, 此时 α_p 长度约为 1.35 μm ,

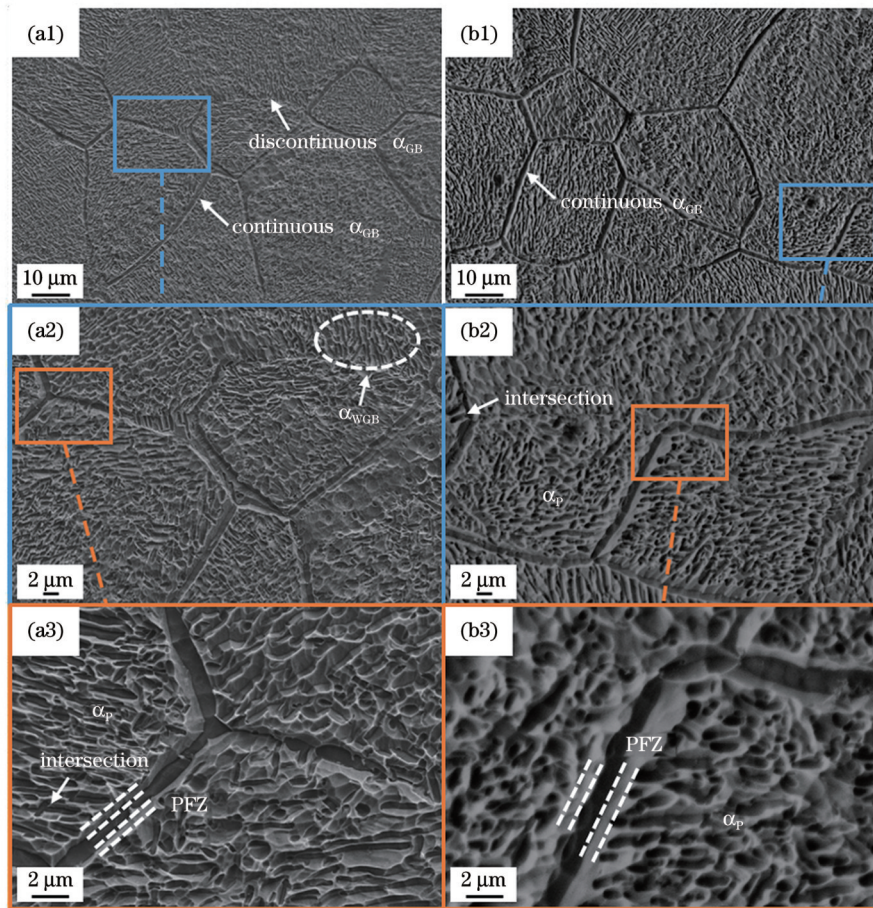


图 7 TC17 合金的微观结构。(a1)~(a3) 840 °C 预退火; (b1)~(b3) 预退火 + 800 °C 固溶

Fig. 7 Microstructures of TC17 alloys. (a1)~(a3) 840 °C pre-annealing; (b1)~(b3) pre-annealing + 800 °C solution

宽度为 $0.29\ \mu\text{m}$, 体积分数从 67.9% 降至 58.4% 。随后进行 $800\ \text{°C}$ 固溶处理, 晶粒平均直径由 $27.2\ \mu\text{m}$ 降至 $25.49\ \mu\text{m}$, 尺寸的变化可能是由以下因素引起的: 1) 取样位置的差异^[31]; 2) α_{GB} 宽度的变化^[32-33]。晶粒内部的 α_{p} 逐渐扁平化。

除了相尺寸的变化, 在不同热处理工艺下, 受元素扩散速率的影响, α_{GB} 逐渐分为连续 α_{GB} 与不连续 α_{GB} , 并且在连续 α_{GB} 周围出现无相析出区 (PFZ), 不连续 α_{GB} 周围析出晶界 Widmanstätten α 相 (α_{WGB})。这是因为 α 核优先在界面能高的高角度晶界 (HAGBs) 处生成, 沿各自优势方向生长, 形成不连续的 α_{GB} , 其中周围的 α 稳定

元素在 β 基体中保持着一定浓度, 为 α_{WGB} 在 α_{GB}/β 界面不稳定处的形核生长创造了条件, 所以无法形成 PFZ; 但厚而连续的 α_{GB} 更容易在低角度晶界 (LAGBs) 处形成, 连续性导致 β 晶界处的 α 稳定元素耗尽, 形成 PFZ^[34-35], 宽度为 $0.4\sim 0.7\ \mu\text{m}$ 。利用 EDS 对固溶样品的连续 α_{GB} 及周围 PFZ 进行线扫描 (图 8), PFZ 无明显 α 相存在, 表现为 Mo、Cr 等 β 稳定元素的含量偏高而 Al 元素含量较低, α_{GB} 元素含量的变化与 PFZ 相反, 具有明显的显微偏析特征, 这与 Zhu 等^[18] 的结果一致。连续 α_{GB} 的融合过程需要消耗大量的 α 稳定元素, 导致周围元素贫化严重, α_{p} 无法在周围形核, PFZ 随 α_{GB} 的生长而扩大。

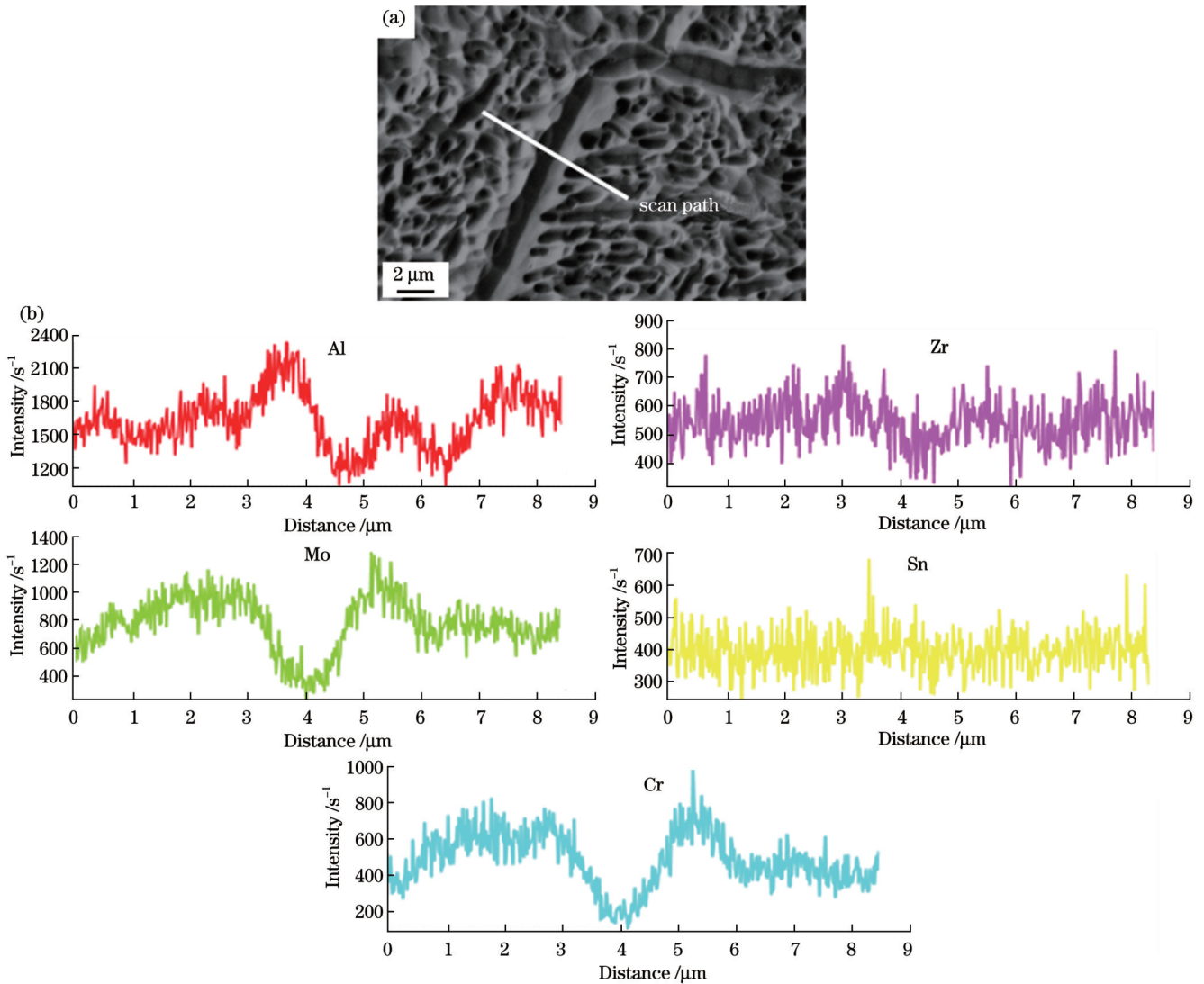


图 8 经 $840\ \text{°C}$ 预退火、 $800\ \text{°C}$ 固溶后扫描路径上 TC17 合金的元素波动。(a) 扫描路径; (b) 元素信号强度

Fig. 8 Elemental fluctuation of TC17 alloy in scanning path after $840\ \text{°C}$ pre-annealing and $800\ \text{°C}$ solution. (a) Scanning path; (b) elemental signal intensity

经预退火与固溶处理后, 分别在 580 、 630 、 $680\ \text{°C}$ 下进行 $8\ \text{h}$ 时效处理, 微观组织如图 9 所示。时效后主要组成相为 β 、 α_{p} 、 α_{GB} 及 α_{s} 。在 $580\ \text{°C}$ 时效后, PFZ 处 β 基体不稳定, 细密的针状 α_{s} 从 PFZ 与 α_{p} 之间的 β 基体上不规则析出, PFZ 消失, 晶粒内部形成 α_{p} 与 α_{s} 混合

区。温度升高至 $630\ \text{°C}$, 时效后一部分极细的 α_{s} 重新溶于 β 基体而另一部分逐渐生长, 但可以观察到 α_{s} 的体积分数下降。在 $680\ \text{°C}$ 时效后, PFZ 重新出现, 只有穿插在 α_{p} 之间的部分粗化 α_{s} 存在。 α_{s} 沉淀在 β 晶粒内部, 取向随机性导致 α_{s} 的尺寸和数量对时效温度的变

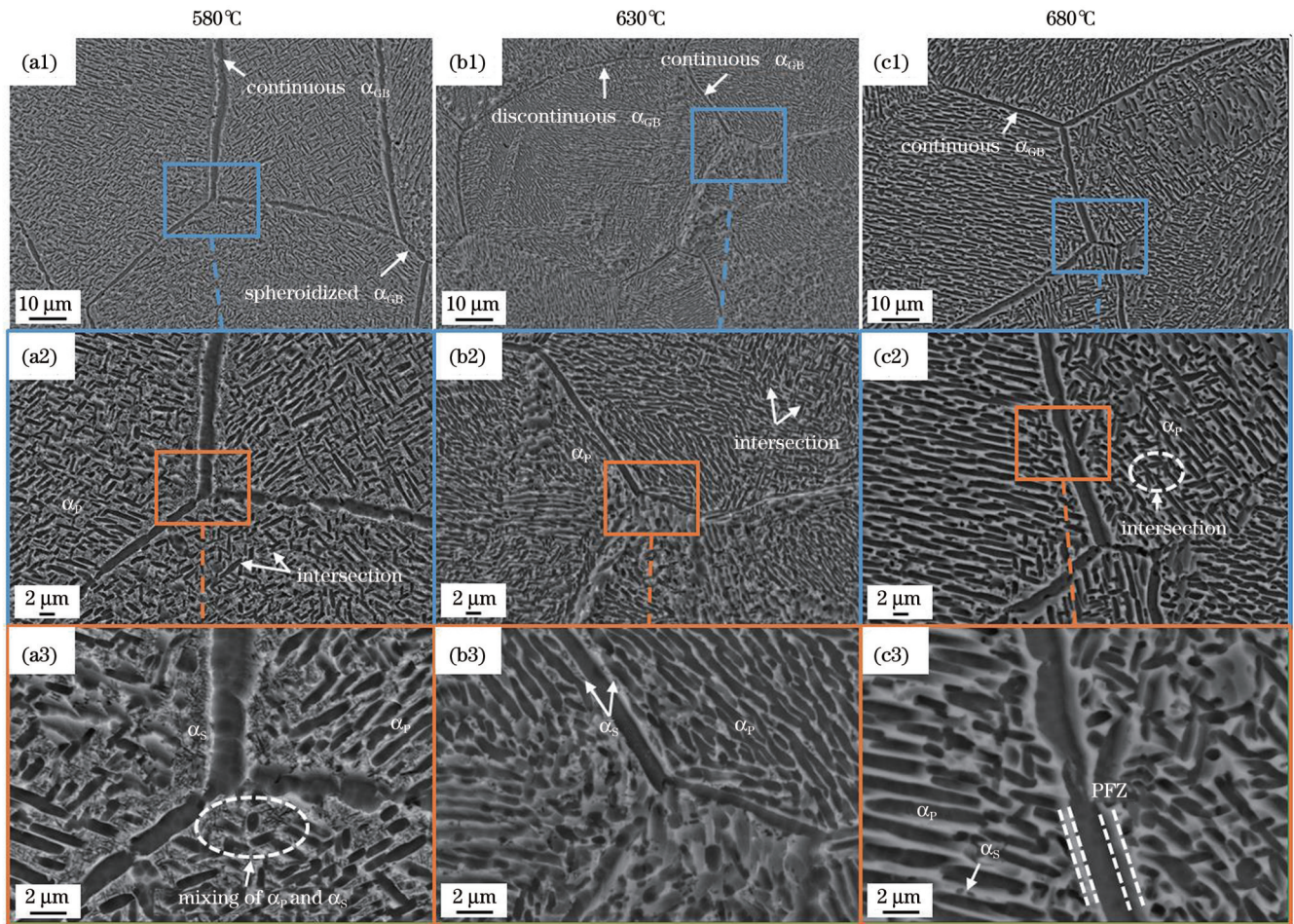


图9 TC17合金经840℃预退火、800℃固溶后在不同时效下的微观结构。(a1)~(a3)580℃时效;(b1)~(b3)630℃时效;(c1)~(c3)680℃时效

Fig. 9 Microstructures of TC17 alloy under different aging conditions after 840℃ pre-annealing and 800℃ solution. (a1)~(a3) 580℃ aging; (b1)~(b3) 630℃ aging; (c1)~(c3) 680℃ aging

化十分敏感,580℃析出时 α_s 相边界十分模糊,难以区分剩余的 β 与 α_s ,温度升高, α_s 的数量减少并且开始粗化,促使相边界逐渐清晰^[36]。与此同时, α_p 也对时效温度表现出一定的敏感性,温度升高促进了 α_p 的生长,提高了扩散速率,当生长速率超过相界面迁移速率时 α_p 开始粗化与球化。

图10总结了沉积与热处理过程中 α 相尺寸及体积分数的变化。在不同温度的时效中,虽然 α_s 、 α_p 与 α_{GB} 不断变化,但 α 相的体积分数维持在66%~69%,达到了平衡状态。时效温度变化不会对 α 相的体积分数产生较大的影响,可知决定 α 相体积分数的是TC17合金成分中 α 稳定元素的含量,与时效温度并无直接关系,但时效温度会影响相的形貌与尺寸,进而影响合金性能。结合不同热处理状态中相的尺寸与形貌及析出与溶解,TC17合金在热处理过程中的微观结构演变如图11所示。

3.3 显微硬度与摩擦学行为

为避免沉积态的杂质影响,每个样品的显微硬度测试了三组数据并取均值,如图12所示。热处理样品的

硬度均高于沉积态,相尺寸与形貌对显微硬度有显著影响。经过840℃预退火、800℃固溶后平均显微硬度达到425.45 HV,略高于沉积态的硬度(~405.45 HV)。硬度受到板条 α 体积分数和尺寸的影响,是相体积分数的强函数^[37]。固溶后 α_p 的析出与生长导致相体积分数增加,从而显微硬度增大。

与固溶后硬度的小幅提升不同,在不同温度时效处理后硬度显著提高,其中580℃时效后达到了最高(~486.93 HV)。时效温度增加但 α 相体积分数稳定(~2.4%),意味在8 h的时间内能够达到两相平衡,相体积分数对时效硬度的影响显著降低。根据对微观组织的分析,时效过程中 α_s 的析出是硬度增大的根本原因。在580℃时效后,取向不一的针状次生相分布在 β 基体上,极大地阻碍了晶格滑移和位错移动,实现了弥散强化,从而导致硬度增大。合金的硬度随着时效温度的升高而降低^[38],这与实验结果一致:在680℃时效后平均硬度为479 HV, α_s 的溶解使相边界减少,削弱了强化效果,且剩余 α_s 板条厚度的增加会导致显微硬度降低^[37],时效过程中 α_p 的生长与球化对硬度的提升

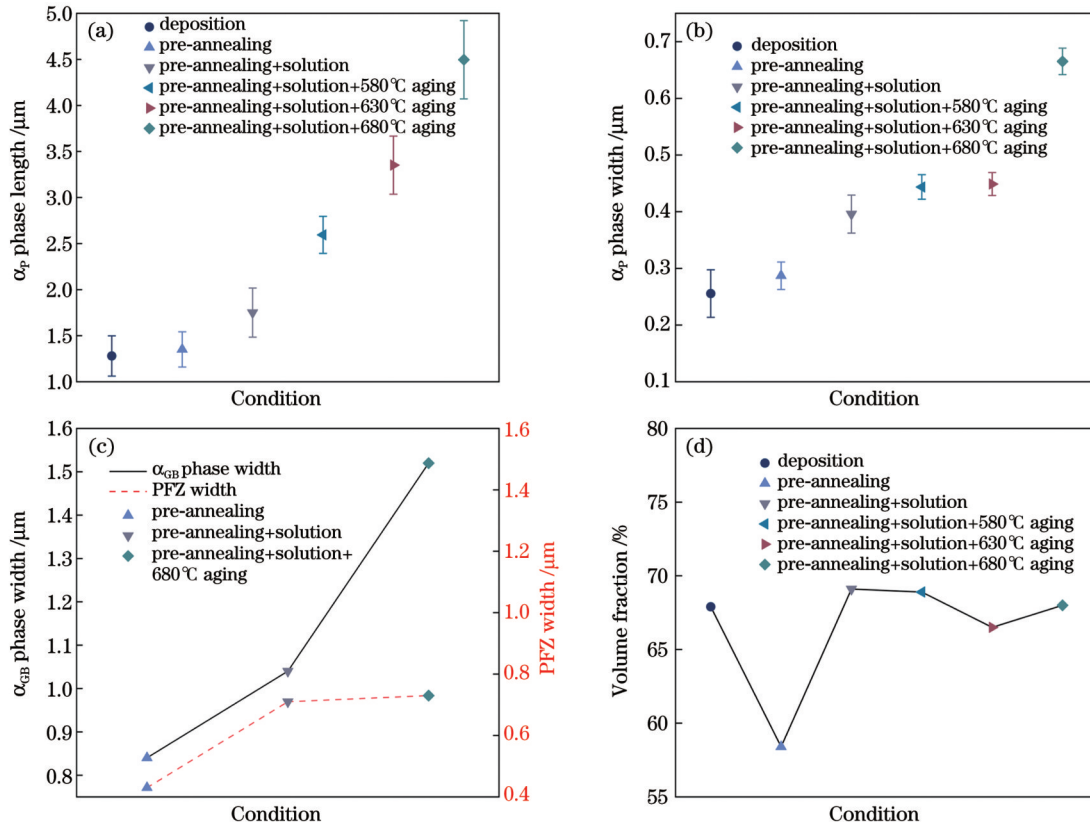


图 10 TC17 合金 α 相的尺寸与体积分数。(a) α_p 相的长度; (b) α_p 相的宽度; (c) α_{GB} 相与 PFZ 的宽度; (d) α 相的体积分数
Fig. 10 α phase sizes and volume fraction in TC17 alloy. (a) Length of α_p phase; (b) width of α_p phase; (c) widths of α_{GB} phase and PFZ; (d) volume fraction of α phase

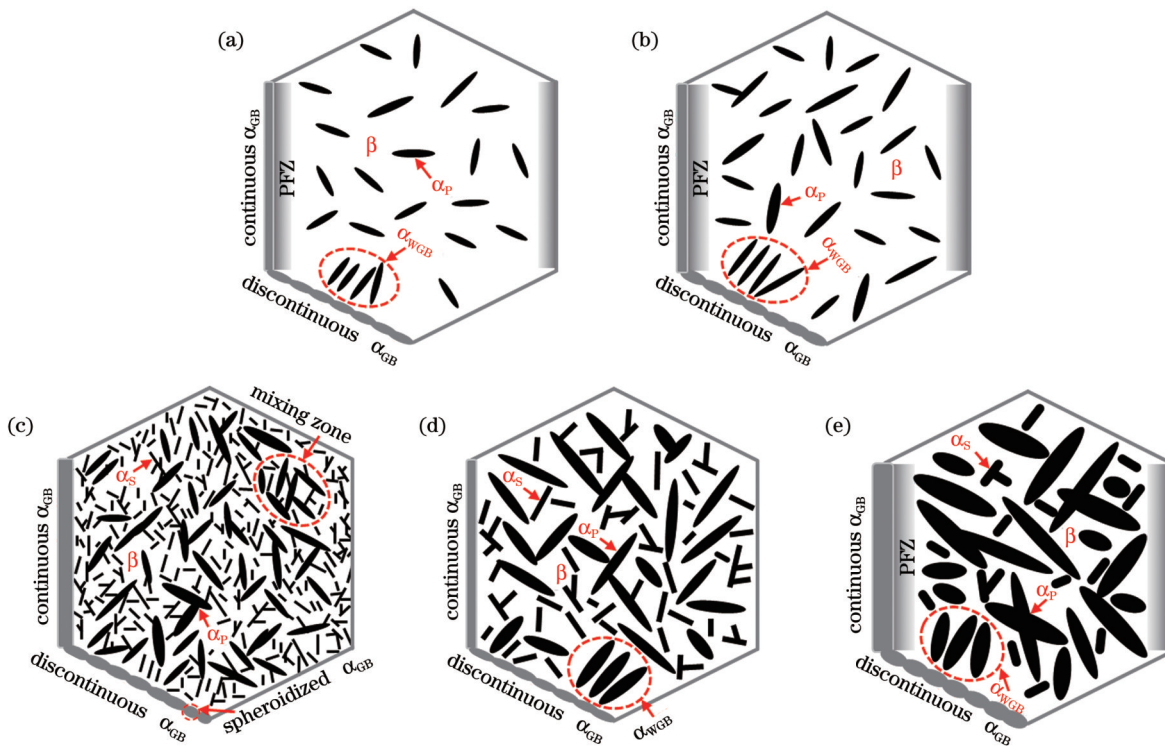


图 11 热处理过程中 TC17 合金的微观组织演变。(a) 预退火; (b) 预退火后固溶; (c) 预退火、固溶后 580 °C 时效; (d) 预退火、固溶后 630 °C 时效; (e) 预退火、固溶后 680 °C 时效
Fig. 11 Microstructure evolution of TC17 alloy during heat treatment. (a) Pre-annealing; (b) solution after pre-annealing; (c) aging at 580 °C after pre-annealing and solution; (d) aging at 630 °C after pre-annealing and solution; (e) aging at 680 °C after pre-annealing and solution

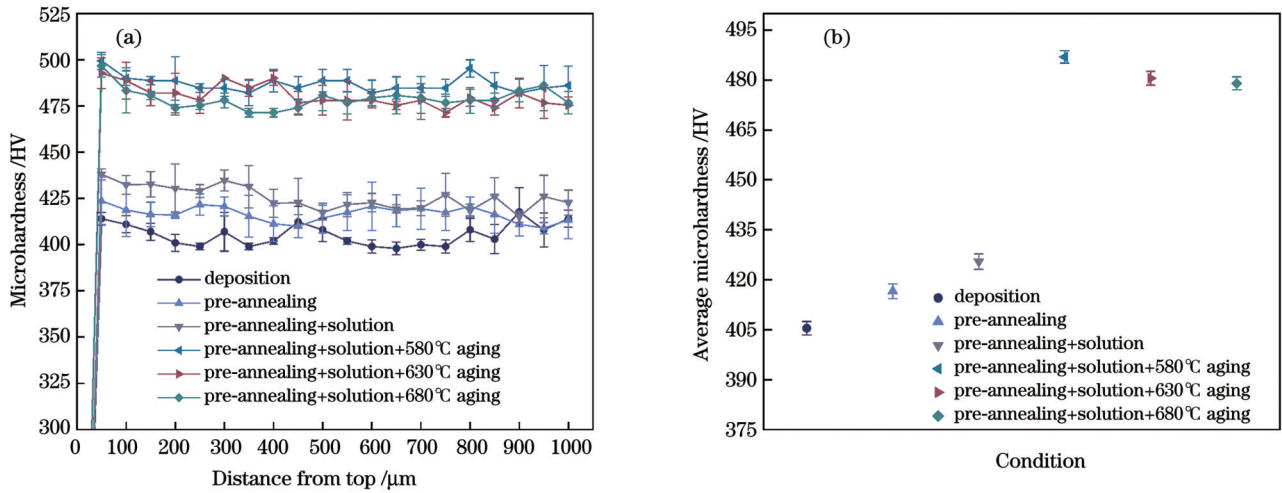


图 12 TC17 合金沉积态与热处理态的显微硬度。(a) 硬度曲线; (b) 平均显微硬度

Fig. 12 Microhardness of TC17 alloys in deposition and heat treatment states. (a) Microhardness curves; (b) average microhardness

效果不明显, 总体硬度下降。

沉积与热处理态的摩擦学性能如图 13 所示。TC17 沉积与热处理态都存在两个磨损阶段: 初始磨损阶段和稳定磨损阶段。在初始磨损阶段, 摩擦系数

的急剧上升主要取决于以下几点: 1) 摩擦副的“冷焊”过程消失后, 表面摩擦力急剧增大, 摩擦系数迅速上升^[39]; 2) 磨损破坏了热处理过程中产生的硬质钛氧化层, 摩擦系数上升。大约摩擦 20 min 后沉积与热处理

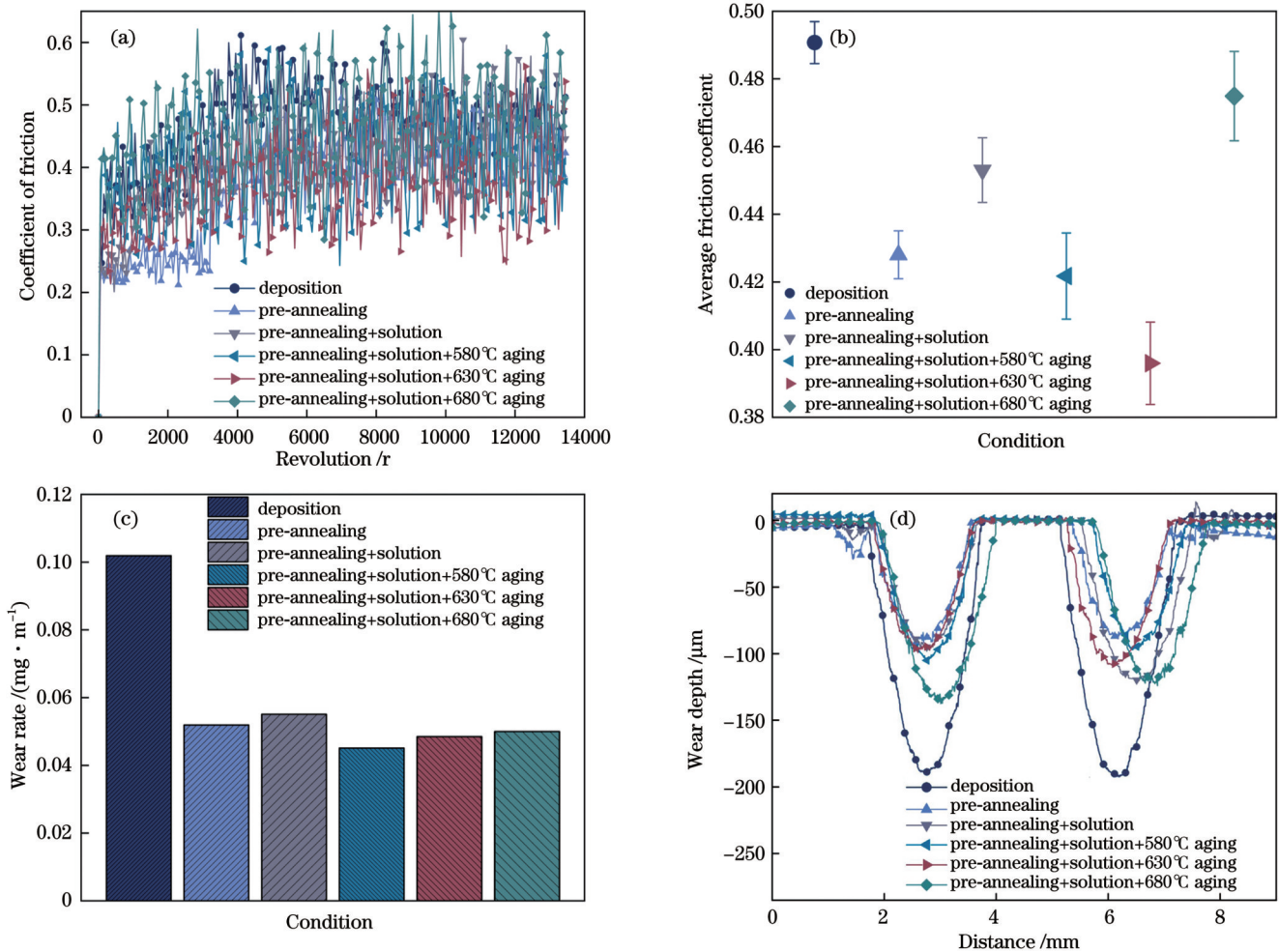


图 13 TC17 合金磨损性能的测试结果。(a) 摩擦系数曲线; (b) 稳定磨损阶段的平均摩擦系数; (c) 磨损率; (d) 二维磨损轮廓

Fig. 13 Test results of wear properties of TC17 alloy. (a) Friction coefficient curves; (b) average friction coefficients during steady wear phase; (c) wear rate; (d) two dimensional wear profile

态均进入持续的稳定磨损阶段,此时摩擦副接触稳定,摩擦过程中温度、速度及磨损机制的改变导致摩擦系数在一定范围内波动。退火与固溶处理后平均摩擦系数(磨损率)分别为0.428(0.0519 mg/m)、0.453(0.0551 mg/m),均优于沉积态 0.491(0.1019 mg/m),由于沉积态具有较低的硬度,磨损球压入较深,材料表面极容易被磨粒剥离,磨损加剧。固溶后的材料比退火后更硬但磨损率升高,这表明热处理后干燥条件下的耐磨性受微观组织的影响比较大,可能PFZ宽度的增加导致塑性降低^[40-41],耐磨性能降低。

580℃时效、630℃时效、680℃时效后摩擦系数(磨损率)分别为0.422(0.0451 mg/m)、0.396(0.0485 mg/m)、0.475(0.050 mg/m),相较于上阶段的固溶处理,耐磨性明显提高,这是由于:1)时效后硬度显著提高,此时抵抗划伤与磨损的能力增强,材料不易剥落;2)次生相在晶界和晶内形成,随机分布的强化相阻碍了位错移动与裂纹扩展,界面强化效果增加。随着时效温度的升高,硬度下降,α_p的粗化与α_s的溶解对位错运动的阻碍作用降低^[42],PFZ使塑性变形更加容易,从而导致耐磨性逐渐降低,但同时硬质氧化层对磨损起到阻碍作用,多因素作用下磨损率小幅度上升(~0.0049 mg/m)。一般来说,摩擦学性能下降时摩擦系数会升高,但630℃时效后磨损率上升、摩擦系数下降,这可能是主导的磨损机制发生了变化,进而影响了摩擦系数^[43]。表3给出了最大磨损宽度和磨损深度,与磨损率的变化趋势一致。

为了进一步研究 TC17 沉积与热处理态的磨损机

表3 TC17合金沉积与热处理态的最大磨损宽度和深度
Table 3 Maximum wear widths and depths of TC17 alloys in deposition and heat treatment states

Condition	Wear width / mm	Wear depth / mm
Deposition	2.056	0.192
Pre-annealing	2.504	0.093
Pre-annealing+solution	2.538	0.120
Pre-annealing+solution+580℃aging	1.789	0.105
Pre-annealing+solution+630℃aging	1.830	0.108
Pre-annealing+solution+680℃aging	2.039	0.137

理,观察了TC17各种状态的磨损表面,如图14所示。对每种样品的残留片层进行元素分析(表4),氧化片层是所有样品都出现的特征,表明样品都存在氧化磨损。沉积态磨损表面较为光滑,犁沟浅而少,磨损表面带有部分残存的氧化层,氧化磨损是其主要磨损机制。热处理后,磨损表面粗糙度上升,覆盖着致密、不规则、被破坏的氧化层,预退火和固溶处理的磨损表面还存在严重的分层和剥落现象,此时分层磨损与氧化磨损同时存在。经过时效处理后,在磨损表面发现黏附的颗粒状与片状碎屑,黏着磨损严重,且随着时效温度的升高,磨粒的堆积和扩散逐渐严重,导致磨损率增加。此外,能够发现,在预退火与630℃时效后,犁沟较其他样品变得深而多,表明在这两种热处理工艺下,磨料磨损也是主导机制之一。热处理后多

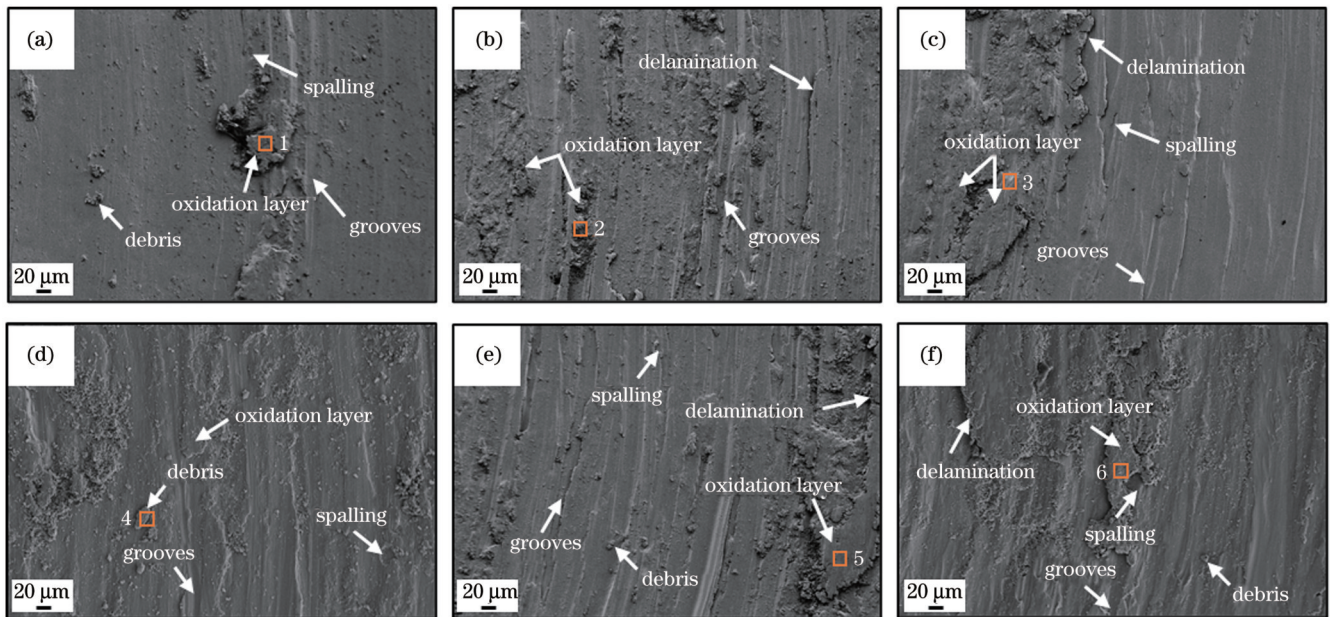


图14 TC17合金沉积与热处理态的磨损表面。(a)沉积;(b)预退火;(c)预退火后固溶;(d)预退火、固溶后580℃时效;(e)预退火、固溶后630℃时效;(f)预退火、固溶后680℃时效

Fig. 14 Wear surfaces of TC17 alloy in deposition and heat treatment states. (a) Deposition; (b) pre-annealing; (c) solution after pre-annealing; (d) aging at 580℃ after pre-annealing and solution; (e) aging at 630℃ after pre-annealing and solution; (f) aging at 680℃ after pre-annealing and solution

表 4 TC17 合金沉积与热处理态氧化层的 EDS 分析
Table 4 EDS analysis results of oxide layer of TC17 alloy in deposition and heat treatment states

Position	Mass fraction / %						
	Al	O	Sn	Zr	Mo	Cr	Ti
1	2.97	7.74	2.17	1.68	2.99	3.55	Bal.
2	3.95	19.9	1.65	1.57	3.25	3.14	Bal.
3	3.96	17.9	1.69	1.58	3.25	3.16	Bal.
4	4.28	14.6	1.93	2.03	3.47	3.18	Bal.
5	2.74	15.2	1.92	1.46	2.91	3.68	Bal.
6	4.14	20.8	1.62	1.83	3.14	3.18	Bal.

种磨损机制共存,形成了氧化、分层、剥落、黏着的粗糙表面形貌。

4 结 论

利用 DED 技术制备了 TC17 沉积试样并对其进行了热处理,研究了热处理过程中相组成、微观结构、显微硬度和摩擦学性能的变化,得到以下结论。

1) 在热处理过程中,TC17 合金主要组织的演变包括: α_p 的生长与粗化; α_{GB} 的连续与不连续生长,其中连续 α_{GB} 周围 PFZ 的宽度与 α_{GB} 的生长呈正向关系; α_s 的析出与生长。随着时效温度的升高,部分 α_s 溶解,部分开始生长,逐渐与 β 相之间形成清晰的相边界, α_p 开始粗化。

2) 热处理态的硬度均大于沉积态。在退火后的固溶阶段, α 相体积分数的增加促使硬度增加;进一步时效后,析出的 α_s 对组织起到弥散强化作用,强化效果随 α_s 的溶解而变弱。其中,580 °C 时效后有更显著的强化效果,硬度比沉积态提高了 20.1%。

3) 热处理态的摩擦学性能均优于沉积态。硬度增加、次生相析出与硬质氧化层的生成是摩擦学性能提升的主要原因。在热处理制度为 840 °C/1 h、AC+800 °C/4 h、WQ+580 °C/8 h、AC 时,耐磨性能达到最优,摩擦系数(磨损率)为 0.422(0.0451 mg/m)。

参 考 文 献

- [1] 陈雪鹏,张凌峰,熊毅,等.激光冲击强化对激光增材制造 TC4 钛合金组织和性能的影响[J].中国激光,2022,49(16):1602017.
Chen X P, Zhang L F, Xiong Y, et al. Effect of laser shock peening on microstructure and properties of laser additive manufactured TC4 titanium alloy[J]. Chinese Journal of Lasers, 2022, 49(16): 1602017.
- [2] Su J L, Xie H M, Tan C L, et al. Microstructural characteristics and tribological behavior of an additively manufactured Ti-6Al-4V alloy under direct aging and solution-aging treatments[J]. Tribology International, 2022, 175: 107763.
- [3] 刘炳森,张述泉,张纪奎,等.层间冷却对激光增材制造 TC17 钛合金组织和拉伸性能的影响[J].中国激光,2022,49(14):1402204.
Liu B S, Zhang S Q, Zhang J K, et al. Effect of interlayer cooling on microstructure and tensile properties of TC17 titanium alloy made by laser additive[J]. Chinese Journal of Lasers, 2022, 49(14): 1402204.
- [4] 邓雨亭,李四清,黄旭,等.航空发动机用 β 锻 TC17 钛合金时效析出行为研究[J].航空制造技术,2018,61(9):59-63,70.
Deng Y T, Li S Q, Huang X, et al. Aging precipitate of beta forged TC17 titanium alloy for aero-engine[J]. Aeronautical Manufacturing Technology, 2018, 61(9): 59-63, 70.
- [5] 沈淑馨,高旭,何蓓,等.显微组织对激光增材制造航空发动机用钛合金室温及中温拉伸性能的影响[J].航空科学技术,2022,33(9):66-76.
Shen S X, Gao X, He B, et al. Effect of microstructure on tensile properties of titanium alloy for aero-engine made by laser additive at room temperature and medium temperature[J]. Aeronautical Science & Technology, 2022, 33(9): 66-76.
- [6] Zhang G D, Xiong H P, Yu H, et al. Microstructure evolution and mechanical properties of wire-feed electron beam additive manufactured Ti-5Al-2Sn-2Zr-4Mo-4Cr alloy with different subtransus heat treatments[J]. Materials & Design, 2020, 195: 109063.
- [7] Shi H L, Liu D X, Zhang X H, et al. Effect of plasma electrolytic oxidation on the hot salt corrosion fatigue behavior of the TC17 titanium alloy[J]. Materials and Corrosion, 2022, 73(4): 558-572.
- [8] Shen X H, Zhang D H, Yao C F, et al. Research on parameter identification of Johnson-Cook constitutive model for TC17 titanium alloy cutting simulation[J]. Materials Today Communications, 2022, 31: 103772.
- [9] 金俊龙,陶军,季亚娟,等.TC17 钛合金嵌入式线性摩擦焊接头组织与性能[J].焊接学报,2021,42(5):18-22,98.
Jin J L, Tao J, Ji Y J, et al. Structure and mechanical property of wedge linear friction welding joint of TC17 titanium alloy[J]. Transactions of the China Welding Institution, 2021, 42(5): 18-22, 98.
- [10] An Z B, He W F, Zhou X, et al. On the microstructure, residual stress and fatigue performance of laser metal deposited TC17 alloy subjected to laser shock peening[J]. Materials, 2022, 15(18): 6501.
- [11] Svetlizky D, Das M, Zheng B L, et al. Directed energy deposition (DED) additive manufacturing: physical characteristics, defects, challenges and applications[J]. Materials Today, 2021, 49: 271-295.
- [12] Piscopo G, Iuliano L. Current research and industrial application of laser powder directed energy deposition[J]. The International Journal of Advanced Manufacturing Technology, 2022, 119(11): 6893-6917.
- [13] 刘业胜,韩品连,胡寿丰,等.金属材料激光增材制造技术及在航空发动机上的应用[J].航空制造技术,2014,57(10):62-67.
Liu Y S, Han P L, Hu S F, et al. Laser additive manufacturing technology of metal materials and its application in aero-engine[J]. Aeronautical Manufacturing Technology, 2014, 57(10): 62-67.
- [14] 聂祥樊,龙宽东,刘海雷,等.激光冲击强化对 TC17 表面硬度的影响[J].机械设计与制造,2012(1):198-200.
Nie X F, Long N D, Liu H L, et al. Effect of laser shock peening on surface hardness of TC17 titanium alloy[J]. Machinery Design & Manufacture, 2012(1): 198-200.
- [15] Bai H Q, Zhong L S, Kang L, et al. A review on wear-resistant coating with high hardness and high toughness on the surface of titanium alloy[J]. Journal of Alloys and Compounds, 2021, 882: 160645.
- [16] 林基辉,温亚辉,范文博,等.钛合金表面激光改性技术研究进展[J].金属热处理,2022,47(3):215-221.
Lin J H, Wen Y H, Fan W B, et al. Research progress of laser modification technology for titanium alloy surface[J]. Heat Treatment of Metals, 2022, 47(3): 215-221.
- [17] 范竞一,马迅,李伟,等.医用钛合金表面改性技术研究进展[J].功能材料,2022,53(7):7027-7039.
Fan J Y, Ma X, Li W, et al. Research progress of surface modification technology of medical titanium alloy[J]. Journal of Functional Materials, 2022, 53(7): 7027-7039.
- [18] Zhu Y Y, Chen B, Tang H B, et al. Influence of heat treatments on microstructure and mechanical properties of laser additive manufacturing Ti-5Al-2Sn-2Zr-4Mo-4Cr titanium alloy[J].

- Transactions of Nonferrous Metals Society of China, 2018, 28(1): 36-46.
- [19] Zhang Q, Chen J, Tan H, et al. Microstructure evolution and mechanical properties of laser additive manufactured Ti-5Al-2Sn-2Zr-4Mo-4Cr alloy[J]. Transactions of Nonferrous Metals Society of China, 2016, 26(8): 2058-2066.
- [20] 陈博, 邵冰, 刘栋, 等. 热处理对激光熔化沉积 TC17 钛合金显微组织及力学性能的影响[J]. 中国激光, 2014, 41(4): 0403001. Chen B, Shao B, Liu D, et al. Effect of heat treatment on microstructure and mechanical properties of laser melting deposited TC17 titanium alloy[J]. Chinese Journal of Lasers, 2014, 41(4): 0403001.
- [21] 崔广发, 席明哲, 周昊阳, 等. 点式锻造激光沉积 TC17 钛合金热处理组织与力学性能[J]. 激光与光电子学进展, 2022, 59(3): 0316003. Cui G F, Xi M Z, Zhou H Y, et al. Microstructure and mechanical properties of heat-treated TC17 titanium alloy formed via point-mode forging laser deposition[J]. Laser & Optoelectronics Progress, 2022, 59(3): 0316003.
- [22] Elshaer R N, El-Hadad S, Nofal A. Influence of heat treatment processes on microstructure evolution, tensile and tribological properties of Ti6Al4V alloy[J]. Scientific Reports, 2023, 13: 11292.
- [23] Huang J Y, Zhang W, Fang W P, et al. Tribology properties of additively manufactured Ti6Al4V alloy after heat treatment[J]. Tribology International, 2023, 185: 108485.
- [24] Ju J, Zhao C L, Kang M D, et al. Effect of heat treatment on microstructure and tribological behavior of Ti-6Al-4V alloys fabricated by selective laser melting[J]. Tribology International, 2021, 159: 106996.
- [25] Yao L, He Y Q, Wang Z Q, et al. Effect of heat treatment on the wear properties of selective laser melted Ti-6Al-4V alloy under different loads[J]. Acta Metallurgica Sinica (English Letters), 2022, 35(3): 517-525.
- [26] Guo X R, Zhang J X, Chen B M, et al. Effects of triple heat treatment on microstructure and the dry sliding wear of TC21 titanium alloy[J]. IOP Conference Series: Materials Science and Engineering, 2020, 768: 022067.
- [27] Kaschel F R, Vijayaraghavan R K, McNally P J, et al. *In-situ* XRD study on the effects of stress relaxation and phase transformation heat treatments on mechanical and microstructural behaviour of additively manufactured Ti-6Al-4V[J]. Materials Science and Engineering: A, 2021, 819: 141534.
- [28] Wang D, Wang H, Chen X J, et al. Densification, tailored microstructure, and mechanical properties of selective laser melted Ti-6Al-4V alloy via annealing heat treatment[J]. Micromachines, 2022, 13(2): 331.
- [29] Monshi A, Foroughi M R, Monshi M R. Modified scherrer equation to estimate more accurately nano-crystallite size using XRD[J]. World Journal of Nano Science and Engineering, 2012, 2(3): 154-160.
- [30] Liu C M, Lu Y, Tian X J, et al. Influence of continuous grain boundary α on ductility of laser melting deposited titanium alloys [J]. Materials Science and Engineering: A, 2016, 661: 145-151.
- [31] Luo K Y, Xu X, Zhao Z, et al. Microstructural evolution and characteristics of bonding zone in multilayer laser cladding of Fe-based coating[J]. Journal of Materials Processing Technology, 2019, 263: 50-58.
- [32] Wang C M, Guo Q L, Zhu X T, et al. Effect of post-weld heat treatment on microstructure and property of linear friction welded TC17/TA15 titanium alloy joint[J]. Materials Characterization, 2023, 199: 112799.
- [33] Schmidt P, El-Chaikha A, Christ H J. Effect of duplex aging on the initiation and propagation of fatigue cracks in the solute-rich metastable β titanium alloy Ti38-644[J]. Metallurgical and Materials Transactions A, 2011, 42(9): 2652-2667.
- [34] Sun Z C, Guo S S, Yang H. Nucleation and growth mechanism of α -lamellae of Ti alloy TA15 cooling from an $\alpha + \beta$ phase field[J]. Acta Materialia, 2013, 61(6): 2057-2064.
- [35] Yin L J, Sun Z C, Yin Z K, et al. The formation of precipitate-free zones in β -quenched TC18 titanium alloy during two phase field heat treatment[J]. Materials Characterization, 2023, 199: 112774.
- [36] Wu C, Zhan M. Microstructural evolution, mechanical properties and fracture toughness of near β titanium alloy during different solution plus aging heat treatments[J]. Journal of Alloys and Compounds, 2019, 805: 1144-1160.
- [37] Liang S, Teng J, Li J H, et al. Effect of solution aging heat treatment on microstructure evolution and properties of TC17 titanium alloy formed by laser solid forming[J]. Journal of Materials Engineering and Performance, 2023: 1-13.
- [38] Fan J K, Li J S, Kou H C, et al. Microstructure and mechanical property correlation and property optimization of a near β titanium alloy Ti-7333[J]. Journal of Alloys and Compounds, 2016, 682: 517-524.
- [39] Wang T, Liu X Y, Chen S Y, et al. Study on microstructure and tribological properties of nano/micron TiC/TC4 composites fabricated by laser melting deposition[J]. Journal of Manufacturing Processes, 2022, 82: 296-305.
- [40] Morita T, Asakura K, Kagaya C. Effect of combination treatment on wear resistance and strength of Ti-6Al-4V alloy[J]. Materials Science and Engineering: A, 2014, 618: 438-446.
- [41] Guo L L, Yang F, Lu B X, et al. Microstructure evolution and strength mechanism of metastable powder metallurgy Ti-6554 titanium alloys under different heat treatment conditions[J]. The Journal of The Minerals, Metals & Materials Society, 2023, 75(7): 2497-2510.
- [42] Pang X T, Xiong Z H, Yao C W, et al. Strength and ductility optimization of laser additive manufactured metastable β titanium alloy by tuning α phase by post heat treatment[J]. Materials Science and Engineering: A, 2022, 831: 142265.
- [43] Svahn F, Kassman-Rudolphi Å, Wallén E. The influence of surface roughness on friction and wear of machine element coatings [J]. Wear, 2003, 254(11): 1092-1098.

Microstructure and Tribological Properties of Additively Manufactured TC17 Titanium Alloy Under Different Heat Treatment Processes

Wang Hao^{1*}, Hu Yining², Wang Tao²

¹Engineering Techniques Training Center, Civil Aviation University of China, Tianjin 300300, China;

²College of Aeronautical Engineering, Civil Aviation University of China, Tianjin 300300, China

Abstract

Objective The TC17 alloy has excellent mechanical strength, fracture toughness, and corrosion resistance and is primarily used in the manufacturing of aero engine disk components. Directed energy deposition (DED) can achieve specific location repairs of damaged

parts and 3D printing of complex and large parts. DED of TC17 alloy has been successfully applied to such parts as integral blade disks. However, the low hardness and poor wear resistance of TC17 alloy make it susceptible to fatigue fracture under the harsh use environment of aero engines, which limits its application in the aerospace field. At present, the problems of poor bonding strength, introduction of new defects, and inability to meet various performance requirements in the spraying of hard coatings on titanium alloy surfaces present potential risks and limitations in aerospace applications. Optimized heat treatment has unique advantages in solving these problems. Optimized heat treatment can adjust material properties by adjusting the microstructure. Several studies have been conducted on improving the tensile properties of TC17 by optimizing the heat treatment process, but further research is needed on whether optimized heat treatments can improve the wear resistance of deposited TC17 alloy. Therefore, in this study, the effects of annealing, post-annealing solid solution, and post-annealing solid solution aging treatments on the microstructure, hardness, and tribological properties of deposited TC17 alloy are investigated. The evolution of the structure during heat treatment and the comprehensive wear behavior under 20 N dry sliding wear are analyzed. The results provide a reference for optimizing the tribological properties and heat treatment process of TC17 alloy.

Methods The experimental material is TC17 spherical powder, with an average particle size of 66.6 μm (Fig. 1). The experiment uses the semiconductor laser to generate lasers, and the robot, equipped with coaxial powder feeding, deposits the TC17 powder on the polished TC4 substrate in the argon environment (Fig. 2). The process parameters are optimized: laser power of 1600 W, scanning speed of 10 mm/s, powder feeding rate of 11 g/min, overlap rate of 45%, and center protection gas flow rate of 11 L/min. A TC17 alloy sample (size of 75 mm \times 35 mm \times 12 mm) is obtained using an N-type scanning path. Samples are taken along the direction of laser deposition, with a sample size of 6 mm \times 6 mm \times 6 mm. The TC17 deposition samples are subjected to pre-annealing, annealing solid solution treatment, and annealing solid solution aging treatment (Fig. 3), and the microstructure and wear properties of the TC17 deposition and heat-treated samples are characterized by the X-ray diffraction (XRD), energy-dispersive X-ray spectroscopy (EDS), scanning electron microscope (SEM), hardness tester, and pin-disk-type friction wear testing machine.

Results and Discussions The experimental results indicate that the deposited TC17 alloy consists of α and β phases, displaying a basketweave structure (Fig. 6). After annealing at 840 $^{\circ}\text{C}$, some of the fine α phase dissolves because of the high temperature. After solid solution treatment at 800 $^{\circ}\text{C}$, the primary α phase (α_{p}) in the grain interior gradually flattens. During the annealing and post-annealing solid solution treatment stages (Fig. 7), affected by the diffusion rates of different elements, the grain boundary α phase (α_{GB}) is divided into continuous α_{GB} and discontinuous α_{GB} . A phase-free zone (PFZ) appears around the continuous α_{GB} because of the insufficient concentration of α stabilizing elements at the low-angle grain boundary. After aging at 580 $^{\circ}\text{C}$ based on the post-annealing solution treatment, a large amount of fine needle-like secondary α phase (α_{s}) precipitates, and the PFZ disappears. When the temperature rises to 630 $^{\circ}\text{C}$, some of the ultrafine α_{s} redissolves in the β matrix. After aging at 680 $^{\circ}\text{C}$, PFZ reappears with only partial coarsening α_{s} interspersed between α_{p} (Fig. 9). The α_{s} precipitates inside the β grains, and the randomness of orientation makes the size and quantity of α_{s} very sensitive to changes in aging temperature. After solution treatment, the average microhardness reaches 425.45 HV, which is higher than the hardness in the as-deposited state (Fig. 12). This is attributed to the precipitation and growth of α_{p} , which increase the volume fraction of the phase, thereby improving the microhardness. After aging treatment, the hardness is further increased, reaching its highest value (\sim 486.93 HV) after aging at 580 $^{\circ}\text{C}$. This is caused by the large amount of α_{s} precipitation, which achieves the strongest dispersion-strengthening effect. The wear test results show that the wear properties of the heat treatment state are superior to those of the deposition state (Fig. 13). Table 3 shows the maximum wear widths and depths in different states. The tribological properties are the best after aging at 580 $^{\circ}\text{C}$, which is attributed to the significant increase in hardness and a large number of secondary phases inhibiting dislocation movement and crack expansion. After heat treatment, a variety of wear mechanisms coexist, and the wear rate and wear morphology depend on the changes in the microstructure and oxide layer.

Conclusions A TC17 sample is prepared by DED and then heat-treated. The changes in phase composition, microstructure, microhardness, and tribological properties during heat treatment are studied. The results show that the main microstructure evolution of TC17 alloy during heat treatment includes the growth and coarsening of α_{p} ; the continuous and discontinuous growth of α_{GB} , where the width of PFZ is positively related to the continuous growth of α_{GB} ; and the precipitation and growth of α_{s} , where, as the aging temperature increases, some α_{s} dissolves and some grows to have a clear phase boundary with the β phase. The hardness after heat treatment is higher than that of the deposited state. In the solid solution stage after annealing, the hardness increases with the increase in α phase volume fraction. After further aging, the precipitation of α_{s} achieves dispersion strengthening, and the strengthening effect weakens with the dissolution of α_{s} . The hardening effect is higher at 580 $^{\circ}\text{C}$, and the hardness is increased by 20.1% compared with that of deposition state. The tribological performance after heat treatment is better than that in the deposition state. The increase in hardness, secondary phase precipitation, and hard oxide formation are the main reasons for the improvement of the tribological properties. Optimal wear resistance is achieved in the heat treatment systems of 840 $^{\circ}\text{C}/1$ h, air cooling+800 $^{\circ}\text{C}/4$ h, water quenching +580 $^{\circ}\text{C}/8$ h, and air cooling, with a friction coefficient (wear rate) of 0.422 (0.0451 mg/m).

Key words laser technique; titanium alloy; tribological properties; microstructure; heat treatment; directed energy deposition